Macromolecules

pubs.acs.org/Macromolecules Article

Topological Frustration as a New Parameter to Tune Morphology Revealed through Exploring the Continuum between A-B-C 3-Arm Star and Linear Triblock Polymers

Rohit Gupta, Mayank Misra, Wenxu Zhang, Ankita Mukhtyar, Samuel P. Gido, Alexander Ribbe, Fernando A. Escobedo, and E. Bryan Coughlin*

Cite This: *Macromolecules* 2021, 54, 4401−4411 Read Online

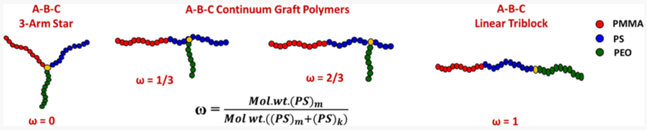

ABSTRACT: Block polymers assemble into a variety of phase-separated morphologies based on volume fraction (φ) and interactions (χ) of the respective blocks. The arrangement of three different polymer blocks could either be a 3-arm star, with each block having one terminus attached to a common junction point or a linear A-B-C architecture. A versatile strategy is reported to synthesize a series of well-defined graft polymers that lie along the unexplored continuum between a 3-arm star and an A-B-C linear triblock polymer architecture. Using the technique of single-molecule insertion, precise control over the position of graft arm C along the B chain was achieved. A series of discrete graft polymers (PMMA-*b*-PS-*g*-PEO) with fixed φ and prescribed ω values that lie on the continuum between a 3-arm star ($\omega = 0$) and linear triblock polymer ($\omega = 1$) were synthesized. Morphological studies using small-angle X-ray scattering and conventional and energy-filtered transmission electron microscopy reveal the transition between lamellae, perforated lamellae, and cylindrical morphologies with systematic variation in the ω values, a trend attributed to the topological frustration and the associated χ values between the three blocks. Molecular dynamic simulations of coarse-grained models were found to predict phase diagrams that are consistent with the experimentally observed morphologies. Our results suggest that changes in ω lead to topological frustration which is an important additional new design parameter that can be used to tune the morphology of multiblock polymers in addition to φ and χ.

■ INTRODUCTION

Block polymers represent a class of materials composed of two or more covalently attached incompatible polymers which spontaneously segregate into self-assembled structures with controllable dimensions and functionalities.[1−4] Morphologies observed for block polymers have been shown to enhance their toughness, stress at failure, and creep resistance.[4,5] The simplest block polymer architecture is the A-B diblock, where morphology is dependent on three experimentally controllable factors: the overall degree of polymerization (N), defined by the molecular weight of the polymer, the volume fraction of the A component (φ_A), and the Flory−Huggins interaction parameter, χ_{AB}, defined as the enthalpy generated from the difference of like and dislike segment interactions. Depending on the values of φ_A and $\chi_{AB}N$, a diblock polymer can self-assemble into different equilibrium morphologies.[1,3] Altering the morphology can be achieved by either adjusting the molecular weight at a fixed φ_A or by changing φ_A.

The tunability of linear block polymers can be significantly enlarged by increasing the number of blocks, which can phase-separate to form multidomain structures used for gas separation and solar cells,[6−8] water purification membranes,[9,10] fuel cell and batteries,[11−13] and the emerging technology of three-dimensional photonic crystals.[14,15] However, the tuning parameters remain the same (φ and χ). If the compositional blocks remain the same (χ is constant), then adjusting the volume fraction of the blocks (φ), the degree of polymerization N remains the only tunable parameter to alter the morphology. The change in molecular weight often leads to a change in polymer morphology which can lead to a detrimental change in the properties of the material such as stress at failure, viscoelasticity, and transport properties.[4,16,17] In addition, for A_nB_n type polymers, conformational asymmetry can also be used to tune block polymer morphology.[18,19]

Among the various multiblock polymer architectures, the linear triblock polymer and the 3-arm star architecture have been studied extensively, both experimentally and theoretically. Many complex morphologies have been observed for both architectures.[2,4,20−42] The 3-arm star and A-B-C linear triblock architectures have the same constitutional blocks, with the placement of the C block at the junction of an A-B diblock polymer leading to the 3-arm architecture or positioning the C

Received: February 5, 2021
Revised: April 4, 2021
Published: April 20, 2021

https://doi.org/10.1021/acs.macromol.1c00277
Macromolecules 2021, 54, 4401−4411

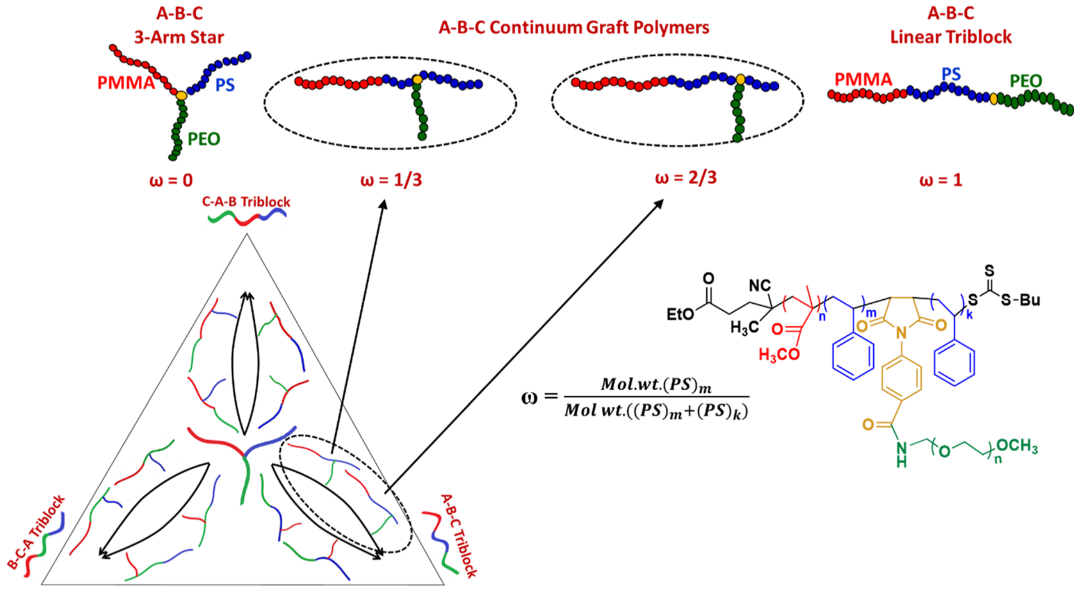

Figure 1. Diagram illustrating the complexity of the possible progression of an A-B-C 3-arm star to linear triblock polymers. The 3-arm star is located at the midpoint of an equilateral triangle, and each vertex represents one of the three possible linear polymer architectures. The continuum graft polymers connecting the central 3-arm star to each vertex can be traversed in two pathways. The expansion shows the investigated continuum progression from the PMMA (red)-*b*-PS (blue)-*g*-PEO (green) A-B-C 3-arm star to A-B-C linear triblock polymer.

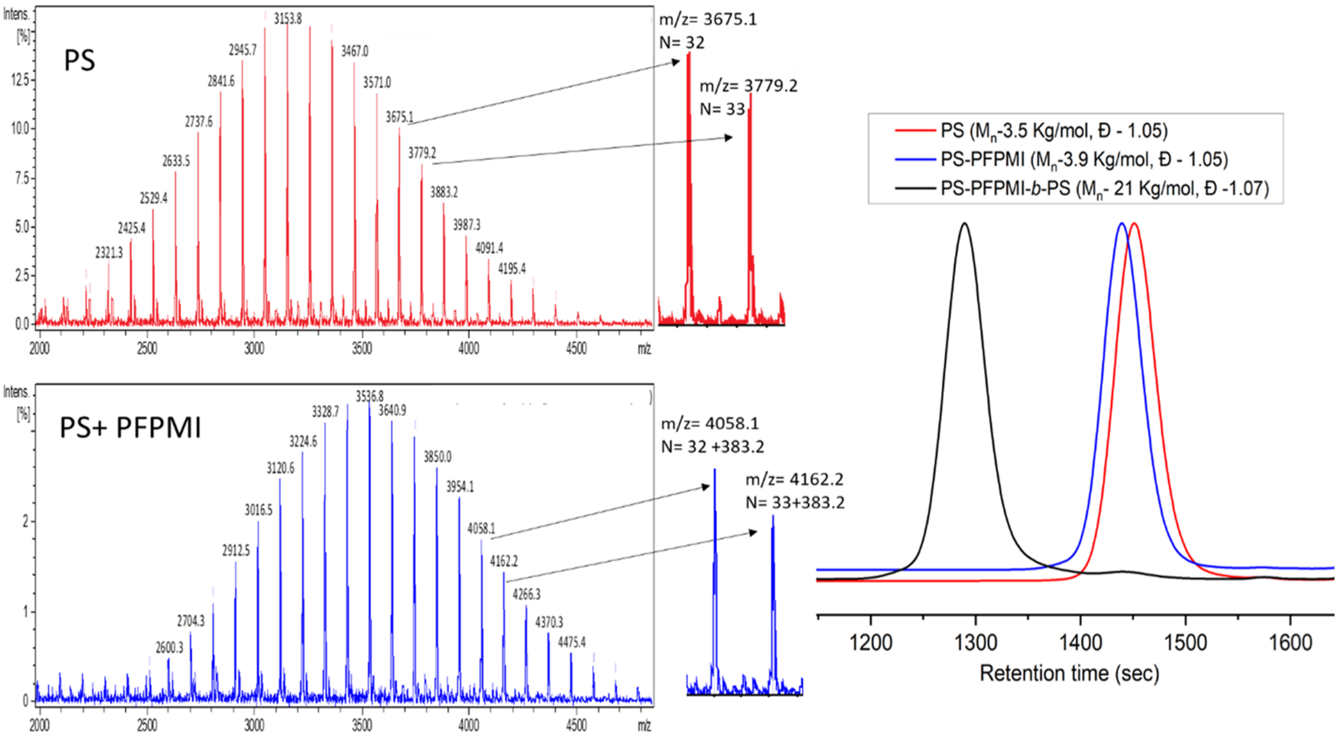

Figure 2. MW distribution of PS chains before and after SMI of PFPMI using ESI-MS (left), GPC traces for PS, PS-PFPMI (right) demonstrating efficient chain extension with styrene after SMI.

block at the terminus of the B block leading to a linear triblock architecture. Conceptually, starting with the 3-arm star, transitioning the position of the C block in discrete intervals along the B arm would ultimately lead to the generation of the A-B-C linear triblock polymer. These unexplored architectures lie along the continuum between a 3-arm star and an A-B-C linear triblock polymer. The structural complexity of such continuum architectures can be represented using an equilateral triangle with the 3-arm star located at the midpoint and each of the vertices representing one of the three possible linear triblock polymer combinations (Figure 1). For the progression from the 3-arm star to each of the different linear triblock polymers, there are two possible pathways to each vertex.

The investigation of these continuum graft polymers first requires the development of suitable synthetic methodologies for the preparation of these novel structures. Full characterization through a combination of experimental and theoretical

Scheme 1. Synthetic Strategy for the Synthesis of PMMA-*b*-PS$_1$-PFPMI-*b*-PS$_2$-*g*-PEO Continuum Graft Polymers

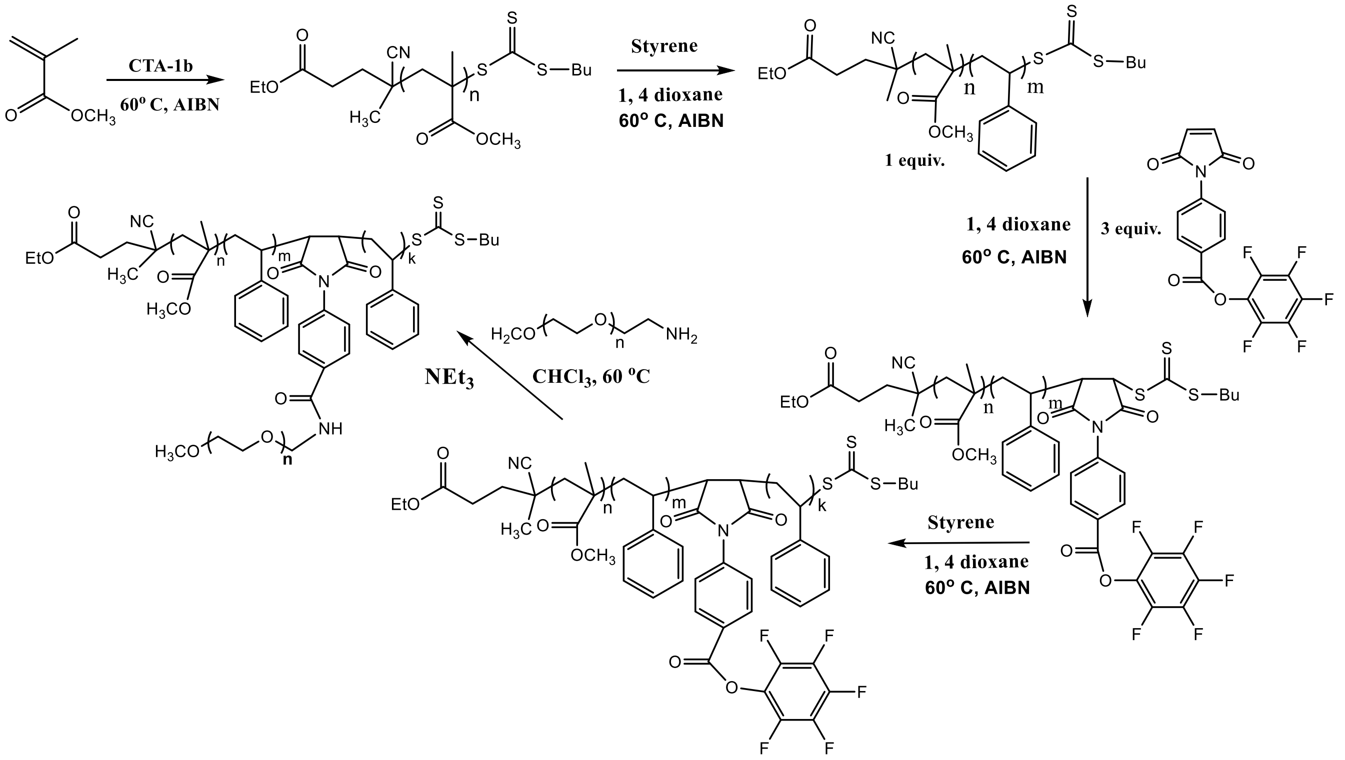

investigations was conducted to reveal the resultant morphologies as a function of graft position along the continuum. As a result of these preparative and characterization investigations, we describe systematic changes in the morphology as a consequence of variation in graft position resulting in topological frustration, all the while keeping the conventional tuning parameters for block polymer morphology χ, N, and φ constant. To test this hypothesis, we investigated one pathway of the progression of an A-B-C 3-arm star to a linear triblock polymer. Utilizing synthetic methodologies, well-defined polymethyl methacrylate (PMMA) (red)-*b*-polystyrene (PS) (blue)-*g*-polyethylene oxide (PEO) (green) continuum graft architectures were prepared (Figure 1) for experimental morphological characterization and predictive theory investigations.

■ RESULTS AND DISCUSSION

Synthesis of PMMA-*b*-PS-*g*-PEO Continuum Graft Polymers. Controlling the monomer sequence can have a profound impact on the overall properties of polymers.[43,44] With the development of controlled polymerization techniques, notable progress has been made in developing protocols to regulate the monomer sequence within polymers.[43,45,46] Using multistep controlled radical polymerization in conjunction with single molecule insertion (SMI), polymer architectures ranging from a 3-arm star, discrete continuum graft polymers, and linear triblock polymers were synthesized. The set of requirements for SMI includes a functional molecule to be inserted only once at the polymer chain-end with high fidelity and maintaining the ability to control subsequent chain extension for a defined polymer chain growth. Additionally, SMI must also provide a site for efficient grafting of the third polymer chain.

Maleimides have a strong preference toward cross-propagation with styrene over homopolymerization.[43,47] In the absence of a styrene monomer, the pentafluoro phenyl ester maleimide (PFPMI) inserts only once at the polymer chain-end with high fidelity. Pentafluoro phenyl esters rapidly undergo quantitative substitution with amine nucleophiles providing a site for efficient grafting.[48] As a proof of concept, the SMI of the PFPMI molecule was performed after the controlled synthesis of a moderate molecular weight (MW) PS as confirmed by ESI-MS where an increase in the MW of the synthesized PS by 383.23 g/mol corresponding to the MW of PFPMI, validating a single insertion of the PFPMI molecule at the PS chain-end (Figure 2). After the successful insertion of PFPMI, the chain extension was performed using styrene as confirmed by ^{1}H NMR and gel permeation chromatography (GPC) (Figure 2, Supporting Information Figure S1). A shift in the molecular weight distribution was observed from 3.9 kg/mol for PS-PFPMI to 21 kg/mol for PS-PFPMI-PS homopolymer with a narrow dispersity (<1.1), confirming the ability of PS-PFPMI chains to initiate controlled growth of PS. This was followed by subsequent grafting of amine-terminated PEO utilizing the activated ester chemistry, confirming the third and final requirement for SMI (Supporting Information Figure S2). Selecting the MW of PS prior to SMI allows for placement of the grafted side chain at specific locations along the continuum.

With the successful demonstration of the SMI technique, we utilized this methodology for the synthesis of discrete PMMA-*b*-PS-*g*-PEO block polymer architectures which lie along the unexplored continuum between a 3-arm star and an A-B-C linear triblock polymer (Scheme 1). For the beginning of the continuum, the synthesis of a 3-arm star was performed by reversible addition fragmentation transfer (RAFT) polymerization to prepare a PMMA homopolymer. Performing the

Table 1. Compositions and Morphologies of the 25-18-ω and 30-32-ω Continuum Graft Polymers[a]

sample ID	PMMA (kg/mol)	PS_1 (kg/mol)	PS_2 (kg/mol)	PEO (kg/mol)	d (nm)	morphology
25-18-0	25	0	25	18	39	perforated lamellae
25-18-1/3	25	8	16	18	30	disordered cylinder
25-18-2/3	25	16	8	18	26	perforated lamellae
25-18-1	25	25	0	18	43	perforated lamellae
30-32-0	30	0	30	32	52	cylinders
30-32-1/3	30	10	20	32	35.3	cylinders
30-32-2/3	30	20	10	32	33	perforated lamellae
30-32-1	30	30	0	32	31.1	cylinders

[a] X-Y-ω; where X denotes the equal MWs of PMMA and PS in a series, Y denotes the corresponding MW of the PEO arm, and ω denotes the grafting position.

SMI with the PFPMI molecule at the chain-end of PMMA (Supporting Information Figure S3), followed by chain extension using styrene, leads to the synthesis of PMMA-PFPMI-PS diblock polymers with an active grafting site at the junction of the two blocks. Utilizing the grafting to approach, an amine-terminated PEO was grafted to the diblock polymer, generating the 3-arm star architecture. Likewise, for the synthesis of the end of the continuum, a controlled radical polymerization of MMA followed by styrene leads to the synthesis of PMMA-*b*-PS, and subsequent SMI of the PFPMI molecule at the active chain-end yields PMMA-*b*-PS-PFPMI. Grafting of amine-terminated PEO generates the linear triblock architecture PMMA-*b*-PS-*g*-PEO. This further demonstrates the versatility of the SMI technique which can be used to synthesize polymer architectures adjusting the location of the SMI on the polymer backbone.

For the synthesis of continuum graft polymers with discrete ω values, PMMA homopolymers and PMMA-*b*-PS_1 diblock polymers with selected MWs were prepared. SMI of PFPMI was performed on the synthesized PMMA-*b*-PS_1 chains, followed by chain extension using styrene to yield PMMA-*b*-PS_1-PFPMI-*b*-PS_2 block polymers. We define the grafting position (ω) for continuum block polymers as the ratio between (PS_1) and (PS_1+ PS_2)

$$\omega = \frac{\text{mol. wt. } (PS_1)}{\text{mol. wt. } (PS_1 + PS_2)}$$

where PS_1 is the PS MW prior to SMI and PS_2 refers to the PS MW after the SMI. Thus, $\omega = 0$ refers to a 3-arm star and $\omega = 1$ refers to a linear triblock polymer. Through a detailed understanding of the polymerization kinetics of styrene polymerization, SMI allows for the synthesis of PMMA-*b*-PS_1-PFPMI-*b*-PS_2 block polymers with prescribed degrees of polymerization of PS_1 and PS_2, resulting in a defined ω value. Amine-terminated PEO was then grafted to the synthesized PMMA-*b*-PS_1-PFPMI-*b*-PS_2 block polymers to yield PMMA-*b*-PS-*g*-PEO continuum graft architectures of exact ω values. To ensure high chemical purity and narrow dispersity of the synthesized continuum graft polymers, selected solvent mixtures were used to remove PMMA, PS, and PEO homopolymer contaminants as described in the Supporting Information.

The chemical and molecular weight characterization of the synthesized continuum graft polymers was performed using ^{1}H NMR, ^{19}F NMR, and GPC (Supporting Information Figures S4 and S5). The ^{1}H NMR signals at $\delta \approx 3.6$ ppm correspond to the methylene proton of the ethyl ester of PMMA and signals between δ values 6−8 ppm correspond to the aromatic protons of PS. After successful grafting of amine-terminated PEO, a new resonance appears at a δ value of 3.65 ppm corresponding to the $-CH_2-CH_2-O-$ protons for the PEO. The individual volume fraction for each polymer block was calculated using ^{1}H NMR by integrating the peak area for specific protons corresponding to the individual blocks. The representative GPC traces for PMMA-*b*-PS-*g*-PEO graft polymers show no homopolymer or diblock contamination, thus demonstrating the high efficiency of this synthetic methodology and the precise control over the molecular weight and dispersity. (Table 1).

MD and Morphological Characterization. Investigation of the phase morphology and evolution kinetics of the materials was performed using a mesoscale molecular dynamics method. Dissipative particle dynamics (DPD) is a simulation technique that typically maps multiple chain "mers" into highly coarse-grained "particles" to study the mesophase formation of block polymers with various molecular architectures.[49−51] Accordingly, DPD can model physical phenomena occurring at the larger time and spatial scales than typical molecular dynamics. DPD incorporates the Flory−Huggins χ parameter by adding a scaling factor a_{ij} to a repulsive conservative potential; that is, $a_{ij} \approx a_{ii} + 3.27\chi_{ij}$, when $a_{ii} = 25$ for a particle number density (ρ) of 3. Accordingly, the scaling factors for our system are $a_{\text{PMMA−PS}} = 40$, $a_{\text{PS−PEO}} = 43.8$, and $a_{\text{PMMA−PEO}} = 25.7$.[52] A bond force ($F^B$) is added to connect bonded DPD particles with a linear spring, $F^B = -kr_{ij}$, where the stiffness constant $k = 4$ in conventional DPD reduced units.[49−51]

To simulate the effect of both grafting position and the molecular weight of PEO on the PMMA-PS backbone, the volume fraction of PMMA and PS is always kept equal by fixing the number of backbone beads to $N = 20$, with $N_{\text{PMMA}} = 10$ and $N_{\text{PS}} = 10$. Due to the coarse grain nature of the model, the grafting point for PEO is considered on the PS_2 segment; hence, the graft position (ω) for simulations is calculated by $N_{PS_1}/N_{(PS_1+PS_2-1)}$ resulting in ω values between 0 for the 3-arm star and 1 for the linear triblock. The simulations were performed in the canonical ensemble (NVT) with a cubic 24 × 24 × 24 box containing 41,472 DPD particles and using periodic boundary conditions. Since the density is kept constant and the molecular weight of PEO is variable, this leads to a variation in the number of molecules in the system. All simulations were initially performed by setting all the interaction parameters a_{ij} as 25, which correspond to an athermal melt. This generates a well-mixed distribution of chains in the simulation box. Then the values of a_{ij} were set to the above-mentioned a_{ij} values representing the appropriate block χ parameters. The system was then allowed to relax to an equilibrated morphology for 5×10^8 time steps. The final state of the simulation was taken as a prediction of the continuum

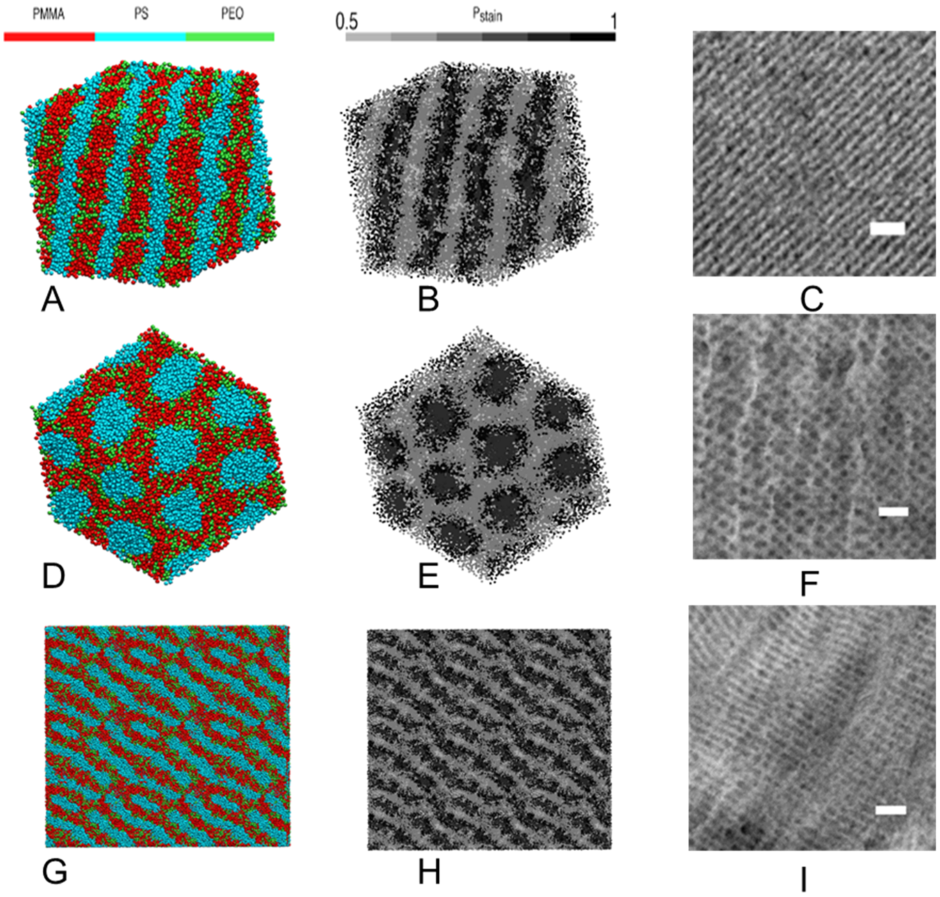

Figure 3. Representative figures for the (a,b) lamellae (d,e) cylindrical, and (g,h) perforated lamellae morphologies observed using DPD simulations and the mimicked contrast through simulations for the experimentally observed morphologies (c,f,i), respectively. Scale bar −100 nm. Image (c) corresponds to 25-8-1 (Supporting Information Figure S7d), (f) corresponds to 30-32-1/3, and (i) corresponds to 30-32-2/3.

graft polymer morphology for comparison to the experimental observations.

Experimental morphological characterization for the different series of graft polymers with varying ω from 0 to 1 was performed using transmission electron microscopy (TEM) and small-angle X-ray scattering (SAXS). For traditional TEM observations, that is, bright-field imaging, ruthenium tetraoxide (RuO_4) was used to stain ultra-microtomed samples. A rationale for the contrast observed on the stained samples is as follows: assuming that the PMMA will decay to some extent due to well-known e-beam instability during room temperature TEM measurements,[53] it will appear as the brightest phase (Supporting Information Table S3) on the TEM images. Since we only consider contrast generated through elastic scattering, the PEO will show the lowest intensity due to the heaviest staining. The PS phase will be mostly unstained and the PMMA phase is not stained by RuO_4.[54,55]

Therefore, we assume that the PEO will be the darkest phase and the PS will have a brightness between PMMA and PEO. For PMMA-*b*-PS-*g*-PEO graft polymers, the progression of χ values is; $\chi_{\text{PMMA-PEO}} < \chi_{\text{PMMA-PS}} < \chi_{\text{PS-PEO}}$. With $\chi_{\text{PMMA-PEO}}$ being small, the PEO chains would prefer mixing with the PMMA chains, but due to the topological frustration in the system, a certain degree of PS-PEO chain mixing is assumed. Since PMMA and PS are immiscible, we only consider the contrast between the PMMA-PEO and PS-PEO mixed phases. Based on these assumptions, the PS-PEO will have a contrast intensity intermediate between PEO and PS, and PMMA-PEO is likely to have a similar contrast to the pure PS phase.

To avoid the uncertainties related to staining, we performed zero-loss energy-filtered TEM (ZL-EFTEM) for the unstained sample series 30-32-ω to obtain a more artifact-free, that is, impact of the heavy metal staining agent,[56] representation of the morphologies formed by these continuum graft copolymers. Postprocessing analysis for both bright-field TEM images of the stained samples as well as the ZL-EFTEM images of the unstained samples was performed by applying two-dimensional-FFT filtering by removing high-frequency noise through the application of a circular mask with a size slightly larger than the respective domain spacings measured by SAXS, that is, all frequencies smaller than the measured expected domain spacings are removed.[57] For the unstained samples, the interpretation is different since the elastic scattering contrast of the three polymers contributes a neglectable amount to the overall contrast. In addition, we assume that both the PMMA and PEO do not experience considerable beam damage under cryo- and low-dose conditions. The compositional differences in the unstained samples appeared adequate to generate sufficient contrast which resembles the morphologies observed for the stained samples as depicted in the Supporting Information Figure S9a−d.

To rationalize the contrast observed via ZL-EFTEM, we consider the following: PEO, as well as PMMA, have 2 oxygens atoms per monomer and almost equal densities (PEO: 1.21 g/cm^3; PMMA: 1.18 g/cm^3); PMMA has 4 carbons in

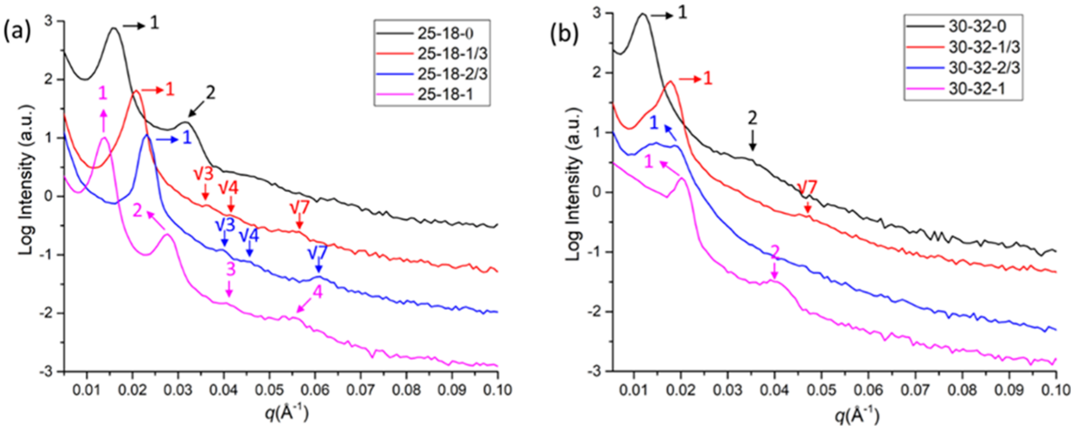

Figure 4. SAXS measurements for (a) 25-18-ω and (b) 30-32-ω series.

comparison to 2 for the PEO per monomer resulting in a higher oxygen density and therefore higher inelastic scattering cross-section for PEO. PEO should therefore appear darker than PMMA in ZL-EFTEM (Supporting Information Table S3). Since PS is only composed of carbon, one could, therefore, expect that it would be the brightest phase in ZL-EFTEM, compared both to PEO and PMMA. Even though the PMMA shows some decay due to electron beam degradation, this contrast will not change. The PS is only composed of carbon, and one could, therefore, expect that it would be the brightest component in EFTEM. PS, however, has an aromatic ring which shows plasmon scattering that might decrease the intensity of the PS phase to some extent. The important conclusion is that whether the PMMA decays or not, it will be the brightest phase and the PEO might be darker than or equally dark as the PS phase. We do not believe that it is reasonable to include mixed phases in these considerations but for the sake of completeness, their intensities should be equal to those observed in the stained samples.

To establish a strong correlation between the morphologies predicted using DPD simulations and those observed by TEM, the representative snapshots for the morphologies predicted are first shown in Figure 3a,d,g and are then processed onto a grayscale in Figure 3b,e,h, respectively. Since the TEM images were obtained by staining the polymer thin film using RuO_4, with staining affinity decreasing from PEO to PS to PMMA, we assigned a RuO_4 staining probability (P_{stain}) to each polymer bead type: $P_{\text{stain}} = \frac{1}{2n}\sum_{i=1}^{n}\alpha_i$, where n is the number of particles in the interaction sphere ($r_c = 1$) and $\alpha_i = 1$, 1.5, and 2 for PMMA, PS, and PEO, respectively. The representative simulated morphologies treated by this staining probability profile suggest that in the morphologies observed by TEM, the PMMA-PEO mixed-phase should appear as the lighter phase and the PS-PEO mixed-phase as the dark phase. These simulated morphologies not only appear similar to the experimentally obtained TEM images (Figure 3c,f,i) but also provide a better understanding of the behavior of the RuO_4 stain for these continuum graft polymers.

For the 25-18-ω series, SAXS data are shown in Figure 4A and TEM in Figure 5a–d. For the 3-arm star (ω = 0), the observation of two SAXS peaks in the ratio of 1:2 could be consistent with any ordered morphology but the corresponding TEM is indicative of a lamellar structure with PMMA-PEO mixed-phase forming one domain while a PS-PEO mixed-phase forming the other domain. Moving along the continuum to graft positions ω = 1/3 and 2/3, weak higher-order SAXS peaks are observed in the sequence 1, $\sqrt{3}$, 2, $\sqrt{7}$. This is suggestive of a hexagonally packed cylindrical morphology or perhaps bcc spheres with the $\sqrt{2}$ peak absent. The TEM image of 25-18-1/3 is most consistent with poorly ordered spherical domains, although it is also possible for disordered, worm-like cylinders to produce such an image with PS-PEO mixed-phase forming the hexagonally packed cylinders within a PMMA-PEO matrix. The poor long-range order evident in the TEM is consistent with the weakness of the higher-order SAXS peaks. TEM images of the 25-18-2/3 morphology (Figure 5c) show a layered structure with morphological complexity within the layers. We conclude that the morphological assignment of a layered structure with a hexagonal arrangement of perforations (responsible for the higher-order SAXS peaks) is most consistent with the data. For the perforated lamellae morphology, the PS-PEO and PMMA-PEO mixed domains form the layered structure with PMMA-PEO perforations running through them. For the linear triblock, 25-18-1, the

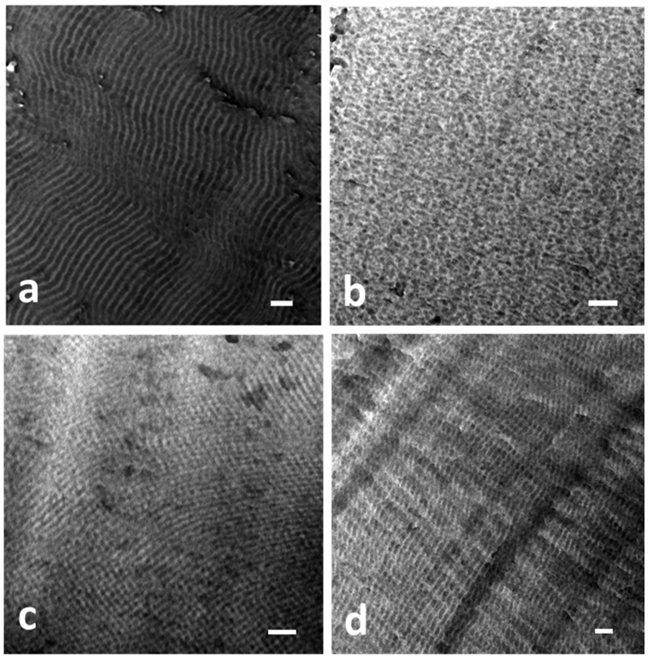

Figure 5. TEM micrographs for different continuum block polymers with varying ω values (a–d) 25-18-ω, ω = 0, 1/3, 2/3, and 1, respectively. Scale bar: 100 nm.

SAXS shows four peaks with q/q^* of 1, 2, 3, and 4 suggesting a layered structure. However, the TEM of this sample shows a complex structure within the layers and in some projections (normal to the layers) hexagonal symmetry is evident. The combination of the SAXS and TEM evidence points to the morphology of hexagonally perforated layers for 25-18-1, with the $\sqrt{3}$ and $\sqrt{7}$ SAXS peaks suppressed due to poor long-range order and/or the form factor.

For the 30-32-ω series, Figure 4B shows the SAXS data and the Supporting Information Figure S9a−d shows representative TEM images. Three of these samples (ω = 0, 1/3, and 1) show higher-order peaks at integral multiples of the primary peak q value. The SAXS data for ω = 0 is suggestive of a layered morphology with a peak ratio of 1:3 which could be consistent with any ordered morphology. However, the corresponding TEM is indicative of a hexagonally packed cylindrical morphology. Similarly, for ω = 1/3, weak higher-order SAXS peaks are observed with a ratio of $1{:}\sqrt{7}$ suggestive of either a hexagonally packed cylinder or bcc-packed spherical morphology. The corresponding TEM images in Figure 3f confirm hexagonally packed cylindrical morphology. The SAXS data for ω = 2/3 only shows the primary peak with the TEM, suggesting a layered morphology with perforations through these layers. For ω = 1, the SAXS data shows higher-order peaks with a ratio of 1:2 suggestive of any ordered morphology but the corresponding TEM images confirm the presence of hexagonally packed cylindrical morphology.

Comparing the two series with the same degree of polymerization of the PEO arm, the 25-18-ω and 30-18-ω series (Supporting Information Figure S6), it can be observed that a small increase in the χN value, can lead to a significant change in the self-assembly behavior of these continuum graft polymers. The domain spacing observed using SAXS for the 25-18-ω decreases from ω = 0 to ω = 2/3 and then starts increasing as the graft position reaches ω = 1.0. However, for the 30-18-ω series, a monotonic decrease in the domain spacing was observed as the graft position for the PEO arm changes from ω = 0 to ω = 1.0. The morphologies observed using TEM for the 25-18-ω, varied from perforated lamellae (ω = 0) to cylindrical morphology (ω = 1/3) then changed to perforated lamellae morphology for the ω values of 2/3 and 1. Whereas, for the 30-18-ω series, the morphology changes from undulated lamellae (ω = 0) to perforated lamellae morphology for ω = 1/3 and 2/3 and back to lamellae morphology for ω = 1. This change in the domain spacing trend using SAXS and the variation in the morphologies observed using TEM with respect to a small increase in the χN value could be attributed to either the presence of a morphological phase boundary of these continuum polymers or the difference in the topological frustration for the two series of graft polymers.

ZL-EFTEM images (Figure 6) for the 30-32-ω series support the morphologies observed using bright-field TEM (Supporting Information Figure S9) and SAXS (Figure 4B). While all samples show matching morphologies, the ZL-EFTEM image for 30-32-1/3 stands apart and provides a more in-depth understanding of the morphological complexity observed for this composition. The domain spacing of the bright-field TEM image in the Supporting Information Figure S9b matches well with the domain spacing of 35 nm observed by SAXS. The ZL-EFTEM image, however, shows an additional spacing in the perpendicular orientation of about 20 nm (the distance of the steps in the "ladder-like" morphology). When taking a closer look at the simulation in Figure 3b, one can see a similar arrangement of PS cylinders in a matrix of PEO/PMMA which appears to show a tendency to phase-separate independently. It is reasonable to assume that the higher step width of the "ladder"-like domains observed in the bright-field TEM image (Supporting Information Figure S9b) is caused by the RuO_4 stain which expands the PEO phase to some extent. We do not observe this spacing in SAXS since PEO and PMMA have the smallest electron density difference of all components (PEO-PMMA = 0.14 vs PEO-PS = 0.57 vs PS-PMMA = 0.42).

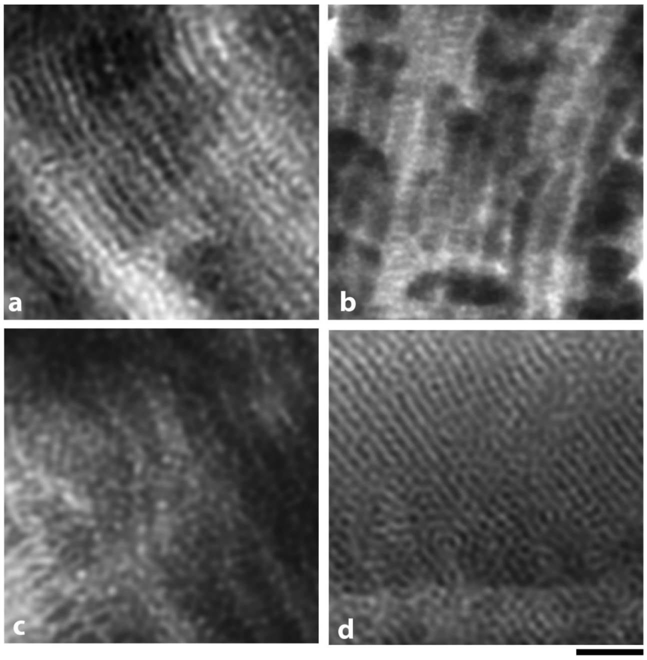

Figure 6. ZL-EFTEM images of unstained samples (a−d) for samples 30-32-0, 30-32-1/3, 30-32-2/3, and 30-32-1. Scale bar for all images: 100 nm.

A comparison between simulated and experimental morphologies for the PMMA-*b*-PS-*g*-PEO graft polymers with respect to changes in ω and φ_{PEO}, where φ_{PEO} is the volume fraction of PEO shows that the morphological transitions predicted for various systems are in qualitative agreement with experimental results based on SAXS and TEM (Figure 7). Three ordered morphologies are observed: lamellae, perforated lamellae, and cylindrical. For the lamellar morphology, a PMMA-PEO mixed-phase formed one domain while a PS-PEO mixed-phase formed the other domain. Similarly, for the cylindrical morphology, the PS-PEO mixed-phase formed the hexagonally packed cylinders within a PMMA-PEO matrix. The formation of a PS-PEO mixed phase for these morphologies can be attributed to the forced mixing of the PS and PEO chains due to topological frustration imposed by the grafting position. In the perforated lamellae morphology, PMMA-PEO and PS-PEO mixed phases formed the lamella domains with PMMA-PEO perforations running through the PS-PEO domains. A few simulated perforated lamellae morphologies initially predicted a continuous PS domain, indicative of a bicontinuous phase, which disappeared on equilibrating for a longer time (5×10^9 time steps).

Altogether, a general morphological trend is observed going from a cylindrical to a lamellar morphology as the chain architecture changes from a 3-arm star to a linear triblock polymer. A similar change in morphology is observed in

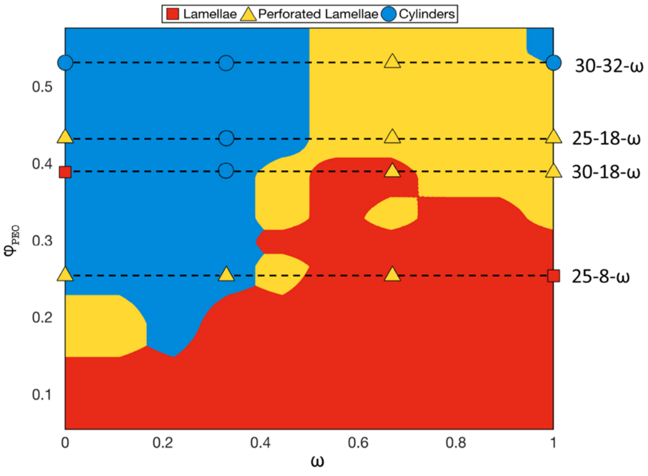

Figure 7. Morphological phase diagram for the PMMA-*b*-PS-*g*-PEO graft polymers obtained from DPD simulations. The symbols represent the morphologies from experimental samples as observed using SAXS and TEM.

diblock polymers, where on reducing the volume fraction of one species relative to another, the morphology changes from lamella to cylinder. However, here we can achieve the same morphology transition without altering the volume fraction in the system by changing the effective interfacial frustration associated with varying ω. Morphologies with increasing interfacial curvature tend to occur for either larger φ_{PEO} at fixed ω or for decreasing ω at fixed φ_{PEO}, wherein with the order of increasing curvature the morphologies are ranked as lamellae < perforated lamella < cylinders. The discrepancies between simulated and experimental results are seen for the star architecture with $\varphi_{\text{PEO}} = 0.39$ and 0.43. These differences may reflect some limitations of the DPD model adopted here whose large extent of coarse graining may blur some important molecular details, for example, in describing the constraints around the grafting point and inaccurately capturing the relative χN interactions.

To further probe the effect of interfacial frustration on moving from a 3-arm star to A-B-C linear triblock polymers, the $\varphi_{\text{PEO}} = 0.31$ system was considered, where a well-defined transition from cylindrical morphology to lamellae was observed in our simulations. We note that near this φ_{PEO} value, the experimental system (i.e., 25-18-ω series) also exhibits a similar high-to-low interfacial-curvature morphological transition upon increasing ω, but rather than transitioning from cylinder to lamellae, the phase shifts from perforated lamellae to lamellae. The calculated fraction of PMMA beads interacting with PEO (Φ_{PMMA}), which quantifies the extent of mixing between these blocks, reveals a slight decrease in their mixing as ω increases (Supporting Information Figure S10). Due to the connectivity to the interphase region between PMMA-PEO, PS-rich domains have a higher concentration of PEO than PMMA-rich domains in the 3-arm star as compared to the linear triblock. The macroscopic morphology change occurs between $\omega = 0.33$ and 0.44, where the cylindrical morphology changes to lamellae morphology and is microscopically marked by a significant increase in the extent of mixing of the fraction of PS with PMMA or PEO (Φ_{PS}). Figure 8a) shows that this trend in Φ_{PS} is expectedly accompanied by increasing potential energy (i.e., energetic penalty) between PS and PMMA + PEO beads.

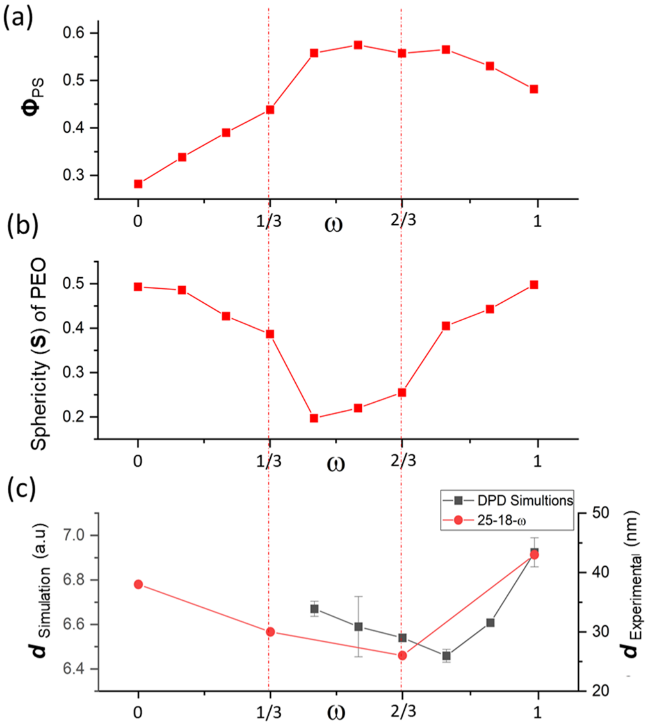

Figure 8. Simulation results for $\varphi_{\text{PEO}} = 0.31$ system: (a) potential energy and the fraction of PS beads (Φ_{PS}) interacting with PMMA or PEO as a function of ω, (b) sphericity of PEO chains, and (c) lamellae thickness for varying ω and its comparison with experimental domain spacing observed using SAXS for the 25-18-ω series.

Since this increased interaction of PS with PEO is energetically unfavorable, it is evident that this phase transition is driven by the small change in the tethering point. This effect emphasizes the idea that morphology can be controlled by changing ω. We hypothesize that the increased mixing of PEO with both PMMA and PS simultaneously is attained by chain stretching of PEO, which would imply an increased conformational frustration in the chain. The extent of chain stretching was measured as the sphericity (S) of the PEO chain[58] defined as $S = 3(\lambda_2 + \lambda_3)/2$, where λ_1, λ_2, and λ_3 are eigenvalues of the inertial tensor and $\lambda_1 > \lambda_2 > \lambda_3$. For a stiff rod-like chain $S \approx 0$ and for an isotropic melt chain $S \approx 1$. A nonmonotonic trend in S for PEO chains as a function of ω (Figure 8b) was observed. As ω increases, the sphericity slightly decreases as the PEO stretches to mix with PMMA; however, at $\omega = 0.44$, a dramatic decrease in S was observed. This decrease in sphericity supports our hypothesis that the chain stretching is coupled to the increased mixing with PMMA: the chain configurational entropic loss (associated with PEO stretching) must be more than compensated by an increase in mixing entropy, which in turn helps stabilize the emerging lamellae phase. The sphericity of PEO in the lamellae morphology starts increasing with ω exhibiting a large jump at $\omega = 0.77$. This increase in sphericity is due to a reduced interaction between PS and PEO, leading to less frustration in the PEO chain. The dramatic change in sphericity at $\omega = 0.77$ is not accompanied by a change in morphology; instead, it is linked to changes in lamellae thickness. Indeed, the lamellae shows a minimum thickness at $\omega = 0.77$ (Figure 8c), which is accompanied by increased mixing of PS with PMMA and PEO. For $\omega > 0.77$, the de-mixing of PS with the other components leads to a rapid increase in lamellae thickness. This trend in lamellae thickness is in qualitative agreement with the *d* spacing trend observed for the 25-18-ω series using SAXS as the lamella phase becomes stable. Overall, the observed changes in lamellae thickness relate to conformational changes in the constituent chains associated with varying degrees of interblock mixing. The sphericity of PMMA, PS_1, and PS_2 was also observed to change with ω but changes were small, and any trend was difficult to discriminate given the large statistical noise in the results. We note that reduction in the sphericity of the PEO segments will also be associated with an increase in chain stiffness which may affect other macroscopic properties like modulus and ionic conductivity.

In conclusion, the SMI of PFPMI and controlled RAFT polymerization provided precise positioning of the third polymer arm to prepare a 3-arm star and an A-B-C linear triblock polymer. Importantly, this highly efficient methodology has been utilized to synthesize novel discrete graft polymers which lie along the continuum between a 3-arm star and an A-B-C linear triblock polymer. The morphological characterization of these novel continuum graft polymers with ω = 1/3 and 2/3 using SAXS and TEM shows a change in morphologies, keeping the φ and χ constant. This approach of architecture tuning by varying ω, leading to topological frustration provides a new design parameter to control block polymer morphology. The DPD simulations provide a more comprehensive understanding of the effect of the full range of ω on the phase behavior of the continuum graft polymers. The morphologies observed for the synthesized continuum graft polymers using SAXS and TEM and the theoretical predictions from DPD simulations are in qualitative agreement. The architectural landscape of the multitude of transitions between a 3-arm star and the linear triblock polymer represented by the ternary diagram in Figure 1 provides extensive possibilities for achieving morphological complexities as a consequence of topological frustration. The validation of the theoretical model built here provides a platform to gain insights into possible combinations of monomers (Figure 1, red, blue, and green), overall MWs, respective volume fraction, and χN values to obtain desirable morphologies. Realizing these structures will require the development of additional molecular candidates for utilization in the SMI technique.

MATERIALS AND METHODS

The details on synthetic procedures for preparation of monomers and polymers, polymer characterization, sample preparation for SAXS, TEM, and ZL-EFTEM, staining procedure, and estimated contrast for TEM and ZL-EFTEM are provided in the Supporting Information. Parameters for the DPD simulations are provided in the Supporting Information.

ASSOCIATED CONTENT

Supporting Information

The Supporting Information is available free of charge at https://pubs.acs.org/doi/10.1021/acs.macromol.1c00277.

> Detailed synthetic procedures for PMMA-b-PS-g-PEO continuum polymers; corresponding GPC, NMR, and ESI characterization data; bright-field TEM images; and phase mixing calculations from DPD simulations (PDF)

AUTHOR INFORMATION

Corresponding Author

E. Bryan Coughlin – *Department of Polymer Science & Engineering, University of Massachusetts, Amherst, Massachusetts 01003-4530, United States*; orcid.org/0000-0001-7065-4366; Email: Coughlin@mail.pse.umass.edu

Authors

Rohit Gupta – *Department of Polymer Science & Engineering, University of Massachusetts, Amherst, Massachusetts 01003-4530, United States*
Mayank Misra – *School of Chemical and Biomolecular Engineering, Cornell University, Ithaca, New York 14853, United States*; orcid.org/0000-0002-2700-1228
Wenxu Zhang – *Department of Polymer Science & Engineering, University of Massachusetts, Amherst, Massachusetts 01003-4530, United States*
Ankita Mukhtyar – *School of Chemical and Biomolecular Engineering, Cornell University, Ithaca, New York 14853, United States*
Samuel P. Gido – *Department of Polymer Science & Engineering, University of Massachusetts, Amherst, Massachusetts 01003-4530, United States*
Alexander Ribbe – *Department of Polymer Science & Engineering, University of Massachusetts, Amherst, Massachusetts 01003-4530, United States*
Fernando A. Escobedo – *School of Chemical and Biomolecular Engineering, Cornell University, Ithaca, New York 14853, United States*; orcid.org/0000-0002-4722-9836

Complete contact information is available at: https://pubs.acs.org/10.1021/acs.macromol.1c00277

Notes

The authors declare no competing financial interest.

ACKNOWLEDGMENTS

Primary support for the syntheses employing single-molecule insertion was provided through the US Department of Energy (DOE), Office of Basic Energy Sciences, and Division of Materials Sciences and Engineering under award DE-SC0014599 to E.B.C. Characterization studies utilized the Core Facilities of the University of Massachusetts Amherst. Computational calculations were supported by NSF DMREF-1922259 and NSF DMR-1609997 to F.A.E.

REFERENCES

(1) Leibler, L. Theory of Microphase Separation in Block Copolymers. *Macromolecules* **1980**, *13*, 1602–1617.
(2) Bates, F. S.; Hillmyer, M. a.; Lodge, T. P.; Bates, C. M.; Delaney, K. T.; Fredrickson, G. H. Multiblock Polymers: Panacea or Pandora's Box? *Science* **2012**, *336*, 434–440.
(3) Bates, F. S.; Fredrickson, G. H. Block Copolymer Thermodynamics: Theory and Experiment. *Annu. Rev. Phys. Chem.* **1990**, *41*, 525–557.
(4) Bates, C. M.; Bates, F. S. 50th Anniversary Perspective: Block Polymers-Pure Potential. *Macromolecules* **2017**, *50*, 3–22.
(5) Ruzette, A.-V.; Leibler, L. Block Copolymers in Tomorrow's Plastics. *Nat. Mater.* **2005**, *4*, 19–31.
(6) Li, G.; Zhu, R.; Yang, Y. Polymer Solar Cells. *Nat. Photonics* **2012**, *6*, 153–161.
(7) Inganäs, O. Organic Photovoltaics over Three Decades. *Adv. Mater.* **2018**, *30*, 1800388.
(8) Jackson, E. A.; Hillmyer, M. A. Nanoporous Membranes Derived from Block Copolymers: From Drug Delivery to Water Filtration. *ACS Nano* **2010**, *4*, 3548–3553.

(9) Abetz, V. Isoporous Block Copolymer Membranes. *Macromol. Rapid Commun.* **2015**, *36*, 10−22.

(10) Werber, J. R.; Osuji, C. O.; Elimelech, M. Materials for Next-Generation Desalination and Water Purification Membranes. *Nat. Rev. Mater.* **2016**, *1*, 16037.

(11) Bouchet, R.; Maria, S.; Meziane, R.; Aboulaich, A.; Lienafa, L.; Bonnet, J.-P.; Phan, T. N. T.; Bertin, D.; Gigmes, D.; Devaux, D.; Denoyel, R.; Armand, M. Single-Ion BAB Triblock Copolymers as Highly Efficient Electrolytes for Lithium-Metal Batteries. *Nat. Mater.* **2013**, *12*, 452−457.

(12) Elabd, Y. a.; Hickner, M. a. Block Copolymers for Fuel Cells. *Macromolecules* **2011**, *44*, 1−11.

(13) Orilall, M. C.; Wiesner, U. Block Copolymer Based Composition and Morphology Control in Nanostructured Hybrid Materials for Energy Conversion and Storage: Solar Cells, Batteries, and Fuel Cells. *Chem. Soc. Rev.* **2011**, *40*, 520−535.

(14) Boyle, B. M.; French, T. A.; Pearson, R. M.; McCarthy, B. G.; Miyake, G. M. Structural Color for Additive Manufacturing: 3D-Printed Photonic Crystals from Block Copolymers. *ACS Nano* **2017**, *11*, 3052−3058.

(15) Kang, Y.; Walish, J. J.; Gorishnyy, T.; Thomas, E. L. Broad-Wavelength-Range Chemically Tunable Block-Copolymer Photonic Gels. *Nat. Mater.* **2007**, *6*, 957−960.

(16) Wang, W.; Lu, W.; Goodwin, A.; Wang, H.; Yin, P.; Kang, N.-G.; Hong, K.; Mays, J. W. Recent Advances in Thermoplastic Elastomers from Living Polymerizations: Macromolecular Architectures and Supramolecular Chemistry. *Prog. Polym. Sci.* **2019**, *95*, 1−31.

(17) Fan, F.; Wang, W.; Holt, A. P.; Feng, H.; Uhrig, D.; Lu, X.; Hong, T.; Wang, Y.; Kang, N.-G.; Mays, J.; Sokolov, A. P. Effect of Molecular Weight on the Ion Transport Mechanism in Polymerized Ionic Liquids. *Macromolecules* **2016**, *49*, 4557−4570.

(18) Milner, S. T. Chain Architecture and Asymmetry in Copolymer Microphases. *Macromolecules* **1994**, *27*, 2333−2335.

(19) Beyer, F. L.; Gido, S. P.; Poulos, Y.; Avgeropoulos, A.; Hadjichristidis, N. Morphology of Vergina Star 16-Arm Block Copolymers and Scaling Behavior of Interfacial Area with Graft Point Functionality. *Macromolecules* **1997**, *30*, 2373−2376.

(20) Chang, A. B.; Bates, C. M.; Lee, B.; Garland, C. M.; Jones, S. C.; Spencer, R. K. W.; Matsen, M. W.; Grubbs, R. H. Manipulating the ABCs of Self-Assembly via Low-χ Block Polymer Design. *Proc. Natl. Acad. Sci. U.S.A.* **2017**, *114*, 6462−6467.

(21) Polymeropoulos, G.; Zapsas, G.; Ntetsikas, K.; Bilalis, P.; Gnanou, Y.; Hadjichristidis, N. 50th Anniversary Perspective: Polymers with Complex Architectures. *Macromolecules* **2017**, *50*, 1253−1290.

(22) Radlauer, M. R.; Sinturel, C.; Asai, Y.; Arora, A.; Bates, F. S.; Dorfman, K. D.; Hillmyer, M. A. Morphological Consequences of Frustration in ABC Triblock Polymers. *Macromolecules* **2017**, *50*, 446−458.

(23) Kumar, R.; Sides, S. W.; Goswami, M.; Sumpter, B. G.; Hong, K.; Wu, X.; Russell, T. P.; Gido, S. P.; Misichronis, K.; Rangou, S.; Avgeropoulos, A.; Tsoukatos, T.; Hadjichristidis, N.; Beyer, F. L.; Mays, J. W. Morphologies of ABC Triblock Terpolymer Melts Containing Poly(Cyclohexadiene): Effects of Conformational Asymmetry. *Langmuir* **2013**, *29*, 1995−2006.

(24) Beckingham, B. S.; Register, R. A. Architecture-Induced Microphase Separation in Nonfrustrated A-B-C Triblock Copolymers. *Macromolecules* **2013**, *46*, 3486−3496.

(25) Löbling, T. I.; Borisov, O.; Haataja, J. S.; Ikkala, O.; Gröschel, A. H.; Müller, A. H. E. Rational Design of ABC Triblock Terpolymer Solution Nanostructures with Controlled Patch Morphology. *Nat. Commun.* **2016**, *7*, 12097.

(26) Millett, P. C. Time-Dependent Ginzburg-Landau Model for Nonfrustrated Linear ABC Triblock Terpolymers. *Phys. Rev. E: Stat., Nonlinear, Soft Matter Phys.* **2015**, *92*, 022602.

(27) Li, W.; Qiu, F.; Shi, A.-C. Emergence and Stability of Helical Superstructures in ABC Triblock Copolymers Emergence and Stability of Helical Superstructures in ABC Triblock Copolymers. *Macromolecules* **2011**, *45*, 503−509.

(28) Nagpal, U.; Detcheverry, F. a.; Nealey, P. F.; de Pablo, J. J. Morphologies of Linear Triblock Copolymers from Monte Carlo Simulations. *Macromolecules* **2011**, *44*, 5490−5497.

(29) Jinnai, H.; Kaneko, T.; Matsunaga, K.; Abetz, C.; Abetz, V. A Double Helical Structure Formed from an Amorphous, Achiral ABC Triblock Terpolymer. *Soft Matter* **2009**, *5*, 2042−2046.

(30) Matsushita, Y.; Hayashida, K.; Dotera, T.; Takano, A. Kaleidoscopic Morphologies from ABC Star-Shaped Terpolymers. *J. Phys. Condens. Matter* **2011**, *23*, 284111.

(31) Chernyy, S.; Kirkensgaard, J. J. K.; Mahalik, J. P.; Kim, H.; Arras, M. M. L.; Kumar, R.; Sumpter, B. G.; Smith, G. S.; Mortensen, K.; Russell, T. P.; Almdal, K. Bulk and Surface Morphologies of ABC Miktoarm Star Terpolymers Composed of PDMS, PI, and PMMA Arms. *Macromolecules* **2018**, *51*, 1041−1051.

(32) Deng, H.; Li, W.; Qiu, F.; Shi, A.-C. Self-Assembled Morphologies of Linear and Miktoarm Star Triblock Copolymer Monolayers. *J. Phys. Chem. B* **2017**, *121*, 4642−4649.

(33) Hayashida, K.; Dotera, T.; Takano, A.; Matsushita, Y. Polymeric Quasicrystal: Mesoscopic Quasicrystalline Tiling in ABC Star Polymers. *Phys. Rev. Lett.* **2007**, *98*, 195502.

(34) Huang, C.-I.; Fang, H.-K.; Lin, C. H. Morphological Transition Behavior of ABC Star Copolymers by Varying the Interaction Parameters. *Phys. Rev. E: Stat., Nonlinear, Soft Matter Phys.* **2008**, *77*, 031804.

(35) Zhang, G.; Qiu, F.; Zhang, H.; Yang, Y.; Shi, A.-C. SCFT Study of Tiling Patterns in ABC Star Terpolymers. *Macromolecules* **2010**, *43*, 2981−2989.

(36) Grason, G. M.; Kamien, R. D. Interfaces in Diblocks: A Study of Miktoarm Star Copolymers. *Macromolecules* **2004**, *37*, 7371−7380.

(37) Hayashida, K.; Saito, N.; Arai, S.; Takano, A.; Tanaka, N.; Matsushita, Y. Hierarchical Morphologies Formed by ABC Star-Shaped Terpolymers. *Macromolecules* **2007**, *40*, 3695−3699.

(38) Yamauchi, K.; Takahashi, K.; Hasegawa, H.; Iatrou, H.; Hadjichristidis, N.; Kaneko, T.; Nishikawa, Y.; Jinnai, H.; Matsui, T.; Nishioka, H.; Shimizu, M.; Furukawa, H. Microdomain Morphology in an ABC 3-Miktoarm Star Terpolymer: A Study by Energy-Filtering TEM and 3D Electron Tomography. *Macromolecules* **2003**, *36*, 6962−6966.

(39) Gemma, T.; Hatano, A.; Dotera, T. Monte Carlo Simulations of the Morphology of ABC Star Polymers Using the Diagonal Bond Method. *Macromolecules* **2002**, *35*, 3225−3237.

(40) Takano, A.; Kawashima, W.; Noro, A.; Isono, Y.; Tanaka, N.; Dotera, T.; Matsushita, Y. A Mesoscopic Archimedean Tiling Having a New Complexity in an ABC Star Polymer. *J. Polym. Sci., Part B: Polym. Phys.* **2005**, *43*, 2427−2432.

(41) Jiang, K.; Zhang, J.; Liang, Q. Self-Assembly of Asymmetrically Interacting ABC Star Triblock Copolymer Melts. *J. Phys. Chem. B* **2015**, *119*, 14551−14562.

(42) Li, W.; Xu, Y.; Zhang, G.; Qiu, F.; Yang, Y.; Shi, A. C. Real-Space Self-Consistent Mean-Field Theory Study of ABC Star Triblock Copolymers. *J. Chem. Phys.* **2010**, *133*, 064904.

(43) Lutz, J.-F.; Ouchi, M.; Liu, D. R.; Sawamoto, M. Sequence-Controlled Polymers. *Science* **2013**, *341*, 1238149.

(44) Matyjaszewski, K. Architecturally Complex Polymers with Controlled Heterogeneity. *Science* **2011**, *333*, 1104−1105.

(45) Lutz, J.-F.; Lehn, J.-M.; Meijer, E. W.; Matyjaszewski, K. From Precision Polymers to Complex Materials and Systems. *Nat. Rev. Mater.* **2016**, *1*, 16024.

(46) Gody, G.; Rossner, C.; Moraes, J.; Vana, P.; Maschmeyer, T. One-Pot RAFT/" Click " Chemistry via Isocyanates: Efficient Synthesis of α -End-Functionalized Polymers. *J. Am. Chem. Soc.* **2012**, *134*, 12596.

(47) Pfeifer, S.; Lutz, J.-F. A Facile Procedure for Controlling Monomer Sequence Distribution in Radical Chain Polymerizations. *J. Am. Chem. Soc.* **2007**, *129*, 9542−9543.

(48) Kakuchi, R.; Zamfir, M.; Lutz, J.-F.; Theato, P. Controlled Positioning of Activated Ester Moieties on Well-Defined Linear Polymer Chains. *Macromol. Rapid Commun.* **2012**, *33*, 54−60.

(49) Padmanabhan, P.; Martinez-Veracoechea, F. J.; Araque, J. C.; Escobedo, F. A. A Theoretical and Simulation Study of the Self-Assembly of a Binary Blend of Diblock Copolymers. *J. Chem. Phys.* **2012**, *136*, 234905.

(50) Gavrilov, A. A.; Kudryavtsev, Y. v.; Chertovich, A. v. Phase Diagrams of Block Copolymer Melts by Dissipative Particle Dynamics Simulations. *J. Chem. Phys.* **2013**, *139*, 224901.

(51) Groot, R. D.; Warren, P. B. Dissipative Particle Dynamics: Bridging the Gap between Atomistic and Mesoscopic Simulation. *J. Chem. Phys.* **1997**, *107*, 4423−4435.

(52) Chen, N.; Yan, L.-T.; Xie, X.-M. Interplay between Crystallization and Phase Separation in PS-b-PMMA/PEO Blends: The Effect of Confinement. *Macromolecules* **2013**, *46*, 3544−3553.

(53) Hiraoka, H. Radiation Chemistry of Poly(methacrylates). *IBM J. Res. Dev.* **1977**, *21*, 121−130.

(54) Huang, P.; Guo, Y.; Quirk, R. P.; Ruan, J.; Lotz, B.; Thomas, E. L.; Hsiao, B. S.; Avila-Orta, C. A.; Sics, I.; Cheng, S. Z. D. Comparison of Poly(Ethylene Oxide) Crystal Orientations and Crystallization Behaviors in Nano-Confined Cylinders Constructed by a Poly(Ethylene Oxide)-b-Polystyrene Diblock Copolymer and a Blend of Poly(Ethylene Oxide)-b-Polystyrene and Polystyrene. *Polymer* **2006**, *47*, 5457−5466.

(55) Trent, J. S.; Scheinbeim, J. I.; Couchman, P. R. Electron microscopy of PS/PMMA and rubber-modified polymer blends: Use of ruthenium tetroxide as a new staining agent. *J. Polym. Sci. Polym. Lett. Ed.* **1981**, *19*, 315−319.

(56) Park, S.; Kim, B.; Xu, J.; Hofmann, T.; Ocko, B. M.; Russell, T. P. Lateral Ordering of Cylindrical Microdomains under Solvent Vapor. *Macromolecules* **2009**, *42*, 1278−1284.

(57) Libera, M. R.; Egerton, R. F. Advances in the Transmission Electron Microscopy of Polymers. *Polym. Rev.* **2010**, *50*, 321−339.

(58) Bjorken, J. D.; Brodsky, S. J. Statistical Model for Electron-Positron Annihilation into Hadrons. *Phys. Rev. D: Part. Fields* **1970**, *1*, 1416−1420.